Implication of Surface Oxidation of Nanoscale Molybdenum Carbide on Electrocatalytic Activity

Journal:	*Journal of Materials Chemistry A*
Manuscript ID	TA-ART-03-2024-001746.R1
Article Type:	Paper
Date Submitted by the Author:	13-May-2024
Complete List of Authors:	Yu, Siying; University of Illinois at Urbana-Champaign, Chemical and Biomolecular Engineering Gautam, Ankit Kumar; University of Illinois Urbana-Champaign, Department of Chemical and Biomolecular Engineering Gao, Di; Tsinghua University, College of Chemical Engineering, Chongqing University, Chongqing 401331 Kuhn, Andrew; Virginia Commonwealth University, Chemical and Life Science Engineering He, Haozhen; University of Illinois Urbana-Champaign Mironenko, Alex ; University of Illinois Urbana-Champaign, Department of Chemical and Biomolecular Engineering Yang, Hong; University of Illinois Urbana-Champaign, Chemical and Biomolecular Engineering

Implication of Surface Oxidation of Nanoscale Molybdenum Carbide on Electrocatalytic Activity

Siying Yu, Ankit Kumar Gautam, Di Gao, Andrew N. Kuhn, Haozhen He, Alexander V. Mironenko,* Hong Yang*

Department of Chemical and Biomolecular Engineering, University of Illinois Urbana-Champaign, 600 S. Mathews Ave., Urbana, IL, 61801, USA

* Corresponding authors: hy66@illinois.edu (HY); alexmir@illinois.edu (AM)

Keywords: molybdenum carbide, oxycarbide, surface oxidation, electrocatalysis, static slab model, ab initio thermodynamics

Abstract

Transition metal carbides, such as molybdenum carbides, are promising substitutes for noble metals as low-cost, durable electrocatalysts. Under ambient conditions, however, these carbides are subject to oxidation due to their oxophilic nature. The partially oxidized surface may possess both oxygen-modulated metallic-like hydrogen adsorption sites and Brønsted-acidic hydroxyl sites. However, the impact of surface oxidation on electrochemical processes such as hydrogen evolution reaction (HER) has rarely been studied. Here, we synthesized β-Mo_2C catalysts and oxidized their surfaces electrochemically to varying extents to study the effects of surface oxidation on HER activity. The degree of surface oxidation was controlled by applying different potential windows to metal carbide catalysts. The samples with a varying degree of surface oxidation were tested for their HER activity. Experimental data indicate the Tafel slope for HER and double-layer capacitance were negatively affected by surface oxidation, particularly due to the loss of carbon and the formation of electrochemically less active surface oxides. The surface oxidation was studied experimentally by X-ray photoelectron spectroscopy, and simulated using density functional theory (DFT), *ab initio* thermodynamics, and charge transfer estimates. Our DFT calculation results suggest Mo_2C surface, partially oxidized after passivation, favors the adsorption of O* from water during the electrochemical oxidation, giving rise to the anodic current. Oxygen atoms preferentially interact with surface C sites, forming stable -C=O species and oxycarbide-like surfaces. A deeper, substitutive oxidation occurs once the CO species desorbs and additional O is absorbed, resulting in kinetically unstable surface structures. The rate-limiting step switches from CO removal step occurring at a potential between 0.28-0.51 V to water dissociation at a potential greater than 0.51 V. Significant CO removal and O* adsorption create surface structure of Mo(IV) oxide, where each Mo atom is coordinated up to six O atoms. The computational results agree well with experimental observations, such as the onset potential (0.6 V) for CO removal. This work helps to unravel the details of evolution of surface sites during an oxidation process of molybdenum carbides along with their effects on catalytic properties and lays the foundation for their practical uses for various applications.

1. Introduction

Early transition metal carbides (TMCs) are promising substitutes for heterogeneous noble metal catalysts in water splitting,[1-3] nitrogen reduction,[4, 5] biomass conversion,[6, 7] as well as in more traditional petrochemical processes such as isomerization, deoxygenation, and hydrogenation. Their platinum-like catalytic properties stem from the interstitial insertion of carbon atoms into the lattice of transition metals, which leads to orbital hybridization and brings about the *d*-band electronic density of states at the Fermi level resembling noble metals.[8, 9] Bulk TMCs may exhibit thermal stability, mechanic strength, outstanding hardness, and corrosion resistance, which in principle make them less likely to suffer from metal leaching in aqueous electrolytes in comparison with metal and alloy electrocatalysts.[10, 11] Making low-cost, durable, and electroactive materials for electrodes has become an important part in the commercialization of electrolyzers in recent years. In this context, various TMC materials have been explored as cathodic electrocatalysts for hydrogen evolution reaction (HER), thanks to their distinct phases and various compositions.[12-16] They also serve as novel substrates for transition metal catalysts, including noble metals.[17-21] With the advancement in nanoengineering methods which are supported by computational methods, structure designs have become critical in studying the surface active sites and reaction mechanisms.[22-25]

The effect of surface oxidation of metal carbides on electrocatalytic activity, however, has not been examined carefully, leaving uncertainty in understanding kinetics for various reactions. Early TMCs, especially those in nanoscale that are relevant to catalysis, are inevitably oxidized under ambient conditions, resulting in a change of catalytic activity. Partially oxidized surfaces of metal carbides possess both oxygen-modulated, metallic-like H-adsorption sites and Brønsted acid hydroxyl sites.[26] The coexistence of diverse active sites offers unique opportunities for creating multifunctional catalysts whose properties can be tuned according to the degree of surface oxidation. For example, a processing with oxygen allows for facile *in situ* controls of acidic sites on 2-5 nm Mo_2C crystallites, where the site densities were reversibly changed by a factor of ~30.[27] The oxygenated molybdenum carbides were reported to exhibit different product selectivity in hydrodeoxygenation and dehydrogenation reactions.[28-32] Controlled oxidation thus plays a pivotal role in determining the relative concentrations of distinct active sites, which might result in completely different reaction pathways.[33] Despite much interest and attempt, there are few reports on method development for controlling the surface oxidation and detailed studies of its impact on catalysis. An insight into controlled oxidation and its relationship with catalytic properties is particularly important for state-of-the-art applications of TMCs in HER, nitrogen reduction reaction (NRR), biomass conversion,[34-38] just to name a few.

In this work, we used an electrochemical approach in surface treatment of β-Mo_2C electrocatalysts and carefully examined the effect of surface oxidation on the electrocatalytic properties towards HER. Hydrogen evolution reaction is chosen because of its sensitivity to the surface structures and its crucial role in the production of green hydrogen. We choose to use electrochemical oxidation of hexagonal phase β-Mo_2C because this process is expected to irreversibly oxidize carbide surfaces at an electrode potential above 0.4 V (*vs.* NHE).[39] Controlled surface oxidation of β-Mo_2C was carried out in an acidic aqueous electrolyte and monitored by cyclic voltammetry (CV). Compared with direct oxidation in air, electrochemical oxidation is largely confined to the surface of electrodes; thus, the degree of oxidation can be controlled by the applied potential window. In this study, for as-prepared β-Mo_2C electrocatalysts, the onset potential of electrochemical oxidation was found to be ~0.6 V (*vs.* RHE, unless otherwise stated) and the current density reached the maximum at ~0.8 V. The oxidized β-Mo_2C electrocatalysts exhibited lowered HER activity with the increased degree of oxidation. The spectroscopic data indicate surface oxycarbide formation upon deposition of oxygen atoms on exposed surface sites at potentials below 0.4 V. Density functional theory (DFT) and *ab initio* thermodynamics calculations indicate that oxygen atoms preferentially interact with surface carbon atoms to form oxycarbide-like surfaces. The rate-limiting step for oxidation also switches from CO removal at a low potential range up to 0.51 V to water dissociation at a higher treatment potential. At a potential above 0.6 V, the surface undergoes further oxidation to form new Mo (VI) species, The oxidation trends agree surprisingly well between experimental observations and computational predictions. Surface metal oxide phases exhibited considerably lower HER activity than those of metal oxycarbides.

2. Experimental

2.1 Materials

Ammonium molybdate (para) tetrahydrate ($(NH_4)_6Mo_7O_{24}\cdot 4H_2O$, 99.9%) was obtained from Alfa Aesar. Ketjen black EC300J was purchased from Akzo Nobel. Methane (CH_4, UHP), hydrogen (H_2, UHP), nitrogen (N_2), compressed air (breathing quality grade), and argon (Ar, UHP) were obtained from Airgas Inc. Ethanol (190 Proof) was bought from Decon Lab, Inc. Nafion 117 solution (~5% in a mixture of lower aliphatic alcohols and water) was purchased from Sigma-Aldrich. Formic acid (HCOOH, 70% Veritas double distilled) and perchloric acid ($HClO_4$, 70% Veritas double distilled) were obtained from GFS Chemicals. All chemicals and reagents were used as received without treatment.

2.2 Synthesis of carbon-supported β-Mo_2C

Carbon-supported β-Mo_2C was prepared using the wet impregnation method, followed by a carburization step. In a typical synthesis, $(NH_4)_6Mo_7O_{24}\cdot 4H_2O$ (756 mg) and carbon black (243 mg) were mixed with 20 mL of deionized (DI) water (Millipore, resistivity of 18.25 MΩ-cm) in a 100 mL flask. The mixture was then heated on a hotplate stirrer (VWR 7x7 Ceramic Hotplate Stirrer 97042-714) at 70 °C (500 rpm) in an oil bath overnight to evaporate most of water. The remaining solids were transferred to a vacuum oven (VWR Symphony Vacuum Oven, Cat. No. 414004-582) and dried at 60 °C for half an hour. The dried solids were ground into a fine powder and loaded into a quartz tube, which was placed in a vertical furnace. The quartz tube was air-tight and was filled with a flowing gas mixture of CH_4/H_2 (flow rate ratio: 8/32; 40 sccm in total). The heating of the furnace was programmed to firstly increase to 300 °C at a rate of 4 °C/min and then increase to 650 °C at a rate of 1 °C/min. The temperature was kept at 650 °C for 2 h, followed by a natural cooling process. After the furnace was cooled to room temperature, the quartz tube was purged by N_2 for 10 min, then by 2% O_2 (a mixture of 10 sccm compressed air and 90 sccm N_2) for 1 h (the passivation step).

2.3 Electrochemical oxidation of carbon-supported β-Mo_2C

A CHI 760E electrochemical workstation was used to carry out all electrochemical measurements. The three-electrode testing system consists of a glassy carbon rotating disk electrode (RDE, Pine Research Instrumentation, 0.196 cm^2 geometric area) as the working electrode, a graphite rod as the counter electrode, and a reversible hydrogen electrode (RHE) as the reference electrode. The controlled electrochemical oxidation was conducted by performing CV in a mixed aqueous electrolyte solution of 0.1 M $HClO_4$ and 0.5 M HCOOH. The solution was purged with Ar for 20 min to remove dissolved oxygen gas. The CV curves were collected in the potential window from -0.025 V to a predetermined value of 0.4, 0.65, 0.75, 0.85, 0.975, and 1.2 V, respectively. All potentials are versus RHE, unless indicated otherwise. The scan rate of CV was 20 mV/s. The RDE rotation speed was set at 900 rpm. In the preparation of working electrodes, 3 mg of the freshly made β-Mo_2C was dispersed in a mixture of 500 μL of DI water, 1500 μL of ethanol, and 6 μL of Nafion 117 aqueous solution. The typical duration of exposure to air of the as-prepared β-Mo_2C between synthesis and electrochemical measurement was within one week. The mixture was sonicated (2510R-DTH Branson) for 5 min to form a homogeneous suspension (ink). A total volume of 10 μL ink was then drop-cast onto the RDE. The ink-loaded electrodes were then dried in air.

To prepare the oxidized samples under different applied potentials for X-ray photoelectron spectroscopy (XPS), we used carbon paper (catalyst geometric area: 1×1 cm^2) instead of RDE as the working electrode in the electrochemical oxidation step. The catalyst loading per geometric area was kept the same as those in the RDE tests.

2.4 Material characterization

Powder X-ray diffraction (XRD) patterns were obtained from Rigaku Miniflex 600 diffractometer equipped with Cu Kα X-ray source (λ =1.54056 Å). Rietveld refinement of the XRD pattern was conducted using a profile fitting software, TOPAS, provided by Bruker Corporation. The volume-weighted mean crystallite size was calculated by the built-in size estimation functions, based on the refinement results. Transmission electron microscopy (TEM) micrographs were obtained using JEOL 2100 Cryo microscope. The high-resolution TEM micrographs and energy dispersive X-ray spectroscopy (EDS) elemental mapping were obtained by ThermoFisher Scientific Talos F200X G2 Scanning Transmission Electron Microscope (STEM). Thermogravimetric analysis (TGA) was conducted using Q50 Thermogravimetric Analyzer from TA Instruments. X-ray photoelectron spectroscopy (XPS) data were obtained using Kratos Axis Supra+ Photoelectron spectrometer. For the preparation of XPS samples, freshly prepared β-Mo_2C was tested in the dry powder form. Oxidized β-Mo_2C samples were loaded on the carbon paper as described in 2.3. The XPS analysis was performed by using CasaXPS software. The identification and interpretation of XPS data were based on those provided in the XPS handbook.[40] The principle of spin-orbit splitting ratio for Mo 3d spectrum, *i.e.*, 2:3 for $3d_{3/2}$ and $3d_{5/2}$, was applied when deconvoluting the peaks.

2.5 Electrochemical measurement for catalytic properties

The electrocatalytic activity toward HER was determined in Ar-saturated 0.1 M $HClO_4$ aqueous electrolyte using the same three-electrode testing system described in section 2.3. The RDE after the electrochemical oxidation was used as the working electrode. Liner sweep voltammetry (LSV) curves were collected in the potential window between 0 and -0.5 V at the scan rate of 20 mV/s. The RDE rotation speed was set at 900 rpm.

The electrochemically active surface area (ECSA) was estimated based on double-layer capacitance measurement. The measurement was carried out in Ar-saturated 0.1 M $HClO_4$ aqueous electrolyte using the same three-electrode testing system described in section 2.3. The CV curves were collected in the potential window between -0.025 and 0.325 V at a scan rate of 10, 20, 30, 40, and 50 mV/s, respectively. The RDE was kept steady during the measurement. The error bars shown are the standard deviations based on three tests on the same sample.

2.6 Computational method

Spin-polarized periodic density functional theory calculations were performed using the Vienna *ab initio* simulation software (VASP 6.2.0).[41-44] The projector-augmented wave method was used to model core-valence electron interactions[45, 46] with a plane-wave cutoff of 450 eV. We employed the PBE[47] exchange-correlation functional with D3[48] corrections for cell and geometry optimizations, followed by single-point, D3-corrected HSE06[49, 50] calculations (with HSE-specific D3 parameters)[50] at the optimized PBE geometries. The first Brillouin zone was sampled using a 14×14×14 Monkhorst-Pack grid[51] for bulk calculations and a 4×5×1 grid for surface calculations. Initial bulk structures were taken from Shrestha et al.[52] for β-Mo_2C ($P6_3/mmc$ space group) and were optimized at our chosen settings, resulting in lattice constants of a=3.018 Å, b=3.016 Å, and c=4.681 Å. These values compare well with the experimental measurements of a=b=3.002 Å and c=4.729 Å.[53] Pymatgen[54] *SlabGenerator*[55] function was used to build the β-Mo_2C(011)-C-terminated surface, found to be dominant at the nanoscale.[52] We used a 3×1 supercell which exposes 6 C and 3 Mo atoms. Atoms in the bottom half of the slab were fixed at their bulk positions during geometry optimization. Free energies at 298.15 K were obtained by treating all adsorbate degrees of freedom as harmonic. All vibrational frequencies less than 100 cm^{-1} were shifted up to 100 cm^{-1}, according to the prescription by Truhlar et al.[56] All geometry manipulations and job submissions were carried out using the ASE package.[57] Transition state energies and geometries were obtained using the climbing-image NEB method[58] and the dimer method,[59] and were confirmed to have one imaginary vibrational frequency. The solvation environment in surface calculations was described using the VASPsol implicit solvent model[60-62] with the default dielectric constant for bulk water. Bader charges[63-65] were computed for surface Mo atoms at various coverages and were converted to oxidation states by recognizing a linear correlation between both properties (see **Figure S1**). Bulk Mo, Mo_2C, and MoO_3 were used as reference systems for Mo(0), Mo(II), and Mo(VI), respectively.

To elucidate the structure and composition of the surface after electrochemical oxidation, we carried out *ab initio* thermodynamics calculations,[66] assuming equilibrium between chemisorbed O* species and bulk water. Under the equilibrium assumption, the history of a sample (*i.e.*, pretreatment) exerts no influence on its final state, making it possible to neglect the passivation pretreatment step in the model. While H_2O can yield several chemisorbed species (O*, OH*, H_2O*, and H*), the scope of this computational study is restricted to O* overlayers, due to the configurational complexity of mixed O*/OH*/H_2O*/H* adlayers. O*-covered surfaces are anticipated to dominate at higher potentials due to the stabilization of proton-electron pairs, resulting in the destabilization of OH* and H* in comparison to O*. Additionally, since H_2O* is a good leaving group that forms relatively weak bonds with transition metal atoms, the presence of H_2O* species is not expected to profoundly affect the electronic properties of the surface, its oxophilicity, and the oxidation extent. Consequently, co-adsorbed H_2O* is neglected in our model. A few exploratory (*i.e.*, non-comprehensive) surface calculations involving OH* and H_2O* were carried out to provide qualitative tests for several hypotheses pertaining to surface structure and stability.

In calculations of the Gibbs free energy of formation of partially oxidized β-Mo_2C(011)-C slabs containing n O* atoms, the following reaction was considered:

$$\mathrm{Mo_xC_y} + n\,\mathrm{H_2O}\ (\mathrm{liq}) \leftrightarrow \mathrm{Mo_xC_y}\big|\mathrm{O_n^*} + 2n(\mathrm{H^+} + \mathrm{e^-}) \qquad (1)$$

The Gibbs free energy of formation was computed as follows:

$$\Delta G_{rxn}^{298.15} = \Big(G\big(\mathrm{Mo_xC_y}|\mathrm{O_n^*}\big) - G\big(\mathrm{Mo_xC_y}\big)\Big) - n\big(G(\mathrm{H_2O}) - 2G(\mathrm{H^+} + \mathrm{e^-})\big) \qquad (2)$$

$G\big(\mathrm{Mo_xC_y}\big)$ was approximated by the electronic energy of a pristine slab. $G\big(\mathrm{Mo_xC_y}|\mathrm{O_n^*}\big)$ contained electronic energy along with O* vibrational contributions to enthalpy and entropy. $G(\mathrm{H_2O})$ was computed for water vapor in the ideal gas state at a temperature of 298.15 K and a saturation pressure of 3169 Pa.[67] No implicit solvation was employed in a DFT calculation of a single H_2O molecule, since the free energy of solvation is already accounted for in the saturation pressure. The computational hydrogen electrode model[68] was used to compute the energy of a proton-electron pair as follows:

$$G(\mathrm{H^+} + \mathrm{e^-}) = \frac{1}{2}G(\mathrm{H_2}) - k_B T \ln(10)\, pH - eU_{SHE} \qquad (3)$$

where $G(\mathrm{H_2})$ is the Gibbs free energy of H_2 ideal gas at 298.15 K and 101,325 Pa, and U_{SHE} is the electrode potential with respect to the standard hydrogen electrode, determined using $U_{SHE} = U_{RHE} - 0.059$ V. Free energies of molecules used in this work are reported in **Table S1**. The pH value of one was used for the entirety of this work. All computational results are reported at U_{RHE} values, unless stated otherwise.

To sample the configurational space in the most computationally efficient way, we adopted the following sequential O* addition procedure. First, we identified the most energetically favorable position of a single O* atom on a pristine β-Mo_2C(011)-C surface, which turned out to be a C site (more favorable than Mo by 0.21 eV at 0 V). Then, keeping the first O* atom fixed, we explored possible configurations for the second O* atom. For the lowest-energy configuration of two O* atoms, the third atom was added at various positions. The sequential approach reduced the search space down to a total of 46 structures. Other computational details can be found in **Note S1~S7** of the Supporting Information.

3. Results and discussion

3.1 Sample preparation and structural characterization

Powder X-ray diffraction (XRD) analysis was performed to confirm the crystal phase of freshly prepared solid samples. All partially oxidized metal carbide samples used in this study were made after a final passivation step to mildly oxidize the surface before their exposure to the ambient environment.[27, 69] [**CAUTION:** Without the passivation, freshly made molybdenum carbide powder samples ignite upon their exposure to ambient air]. The results show the XRD peaks of the freshly made sample match well with the diffraction pattern of hexagonal phase β-Mo_2C (PDF#35-0787) (**Figure 1a**). No extra diffraction peaks were observed, suggesting that the mild oxidation during passivation is limited to the surface and does not affect the bulk phase of metal carbide nanoparticles. The XRD pattern of as-prepared β-Mo_2C did not fit any of the simulated patterns for $(Mo_2C)_xO_y$,[70] ruling out the formation of bulk oxycarbide. It should be noted that the existence of oxycarbide has been confirmed by spectroscopic evidence, though to the best of our knowledge, there is no precise description or experimental confirmation of its atomic structure. The most intense XRD peak observed could be assigned to (101) diffraction of β-Mo_2C, which exhibits a narrower full-width half maximum (FWHM) than those of other diffraction peaks. This result suggests a preferred packing on (101) facet. The measured intensity ratio of (002) to (101) diffractions is close to 0.7, much higher than the value of 0.25 in the standard pattern, which implies a disproportionately higher content of (002) packing in the carbide crystals. The volume-weighted mean crystallite size of β-Mo_2C nanoparticles is estimated to be 5.30±0.07 nm, calculated from Scherrer equation based on the full-profile Rietveld refinement (**Figure S2**).

The TEM micrograph shows the as-prepared β-Mo_2C nanoparticles dispersed across the carbon support (**Figure 1b** and **Figure S3**). The distribution of β-Mo_2C nanoparticles is more evident in the scanning transmission electron microscope (STEM) micrograph (**Figure 1c**). In the dark field TEM, the greyish oval-shaped particle is the carbon support, and the dispersive bright dots indicate regions rich in β-Mo_2C nanoparticles. Energy-dispersive X-ray spectroscopy (EDS) shows the elemental distribution of Mo across the carbon support, which further confirms the formation of well distributed molybdenum carbide nanoparticles (**Figure S4**). We performed TGA to estimate the mass percentage of Mo_2C in the freshly prepared sample, assuming all Mo atoms exist in the form of Mo_2C. There is 67.5 wt.% of MoO_3 in the sample as the combustion product, *i.e.*, the plateau from 580 °C to 700 °C in the weight loss curve (**Figure S5**),[71-73] corresponding to 47.8 wt.% of β-Mo_2C in the freshly prepared, carbon-supported sample.

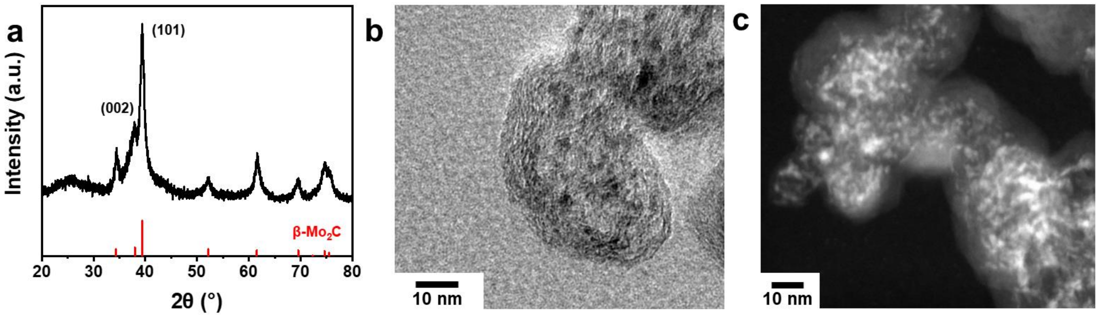

Figure 1. (a) XRD pattern, (b) TEM micrograph, and (c) dark-field STEM image of as-prepared β-Mo_2C nanoparticles on carbon support.

3.2 Electrochemical oxidation and catalytic performance

Controlled surface oxidation of as-prepared β-Mo_2C was monitored by CV in the potential windows between -0.025 V and a predetermined value up to 1.2 V (**Figure 2a**). The results indicate the onset potential of oxidation was about 0.6 V and the peak current density was achieved at the forward potential around 0.8 V. The difference between the onset potential (~0.6 V) and the previously reported value (~0.4 V *vs.* NHE) of carbide planar sheet[39] might be explained by the small size of the as-prepared nanoparticles, which change oxidation kinetics. The CV data show the oxidation current to be close to zero at the forward potential of 1.2 V, suggesting a complete surface oxidation of the metal carbide electrocatalyst. For all CV cycles, the back scans (direction shown by the green arrow in **Figure 2a**) do not exhibit any reduction peaks, indicating the electrochemical oxidation is irreversible. In this study, we name the various electrocatalyst samples as β-Mo_2C-*x*, according to the highest applied potential in V *vs.* RHE used in the electrochemical oxidation process, where *x* is 0.4, 0.65, 0.75, 0.85, 0.975, and 1.2, respectively.

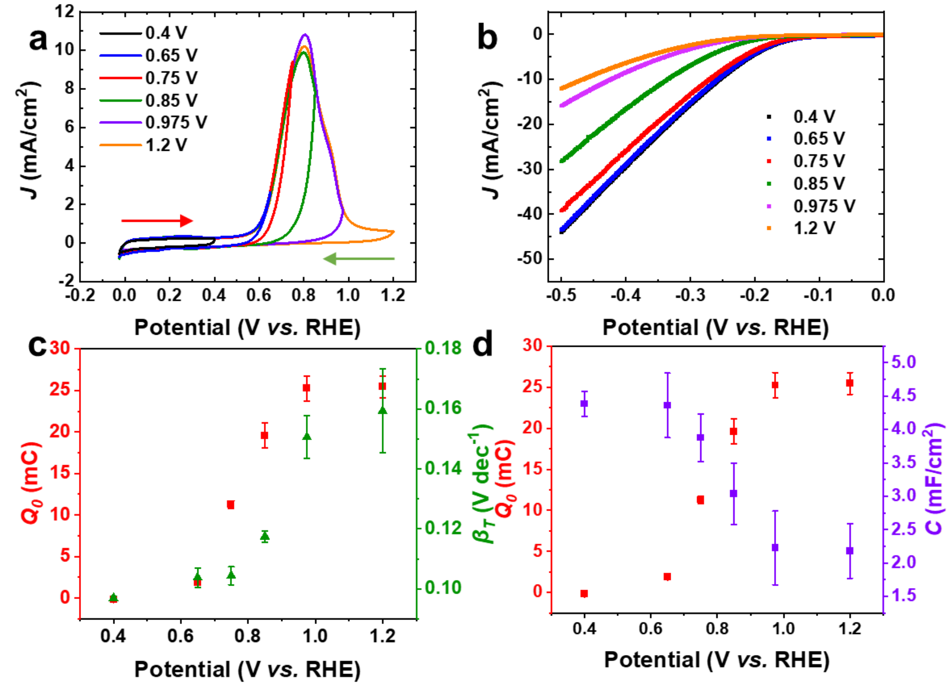

Figure 2. Structure-property relationships of surface-oxidized β-Mo_2C electrocatalysts towards HER. (a) CV curves recorded during the electrochemical surface oxidation (red arrow: direction of the forward scan; green arrow: direction of the back scan). (b) Polarization curves of surface oxidized β-Mo_2C-*x* electrocatalysts for HER. (c) Relationship between total oxidation charges (Q_0) and Tafel slopes (β_T). (d) Relationship between total oxidation charges and capacitance (*C*).

The partially oxidized Mo_2C electrodes were tested for their HER activity by LSV (**Figure 2b**). The HER performance of freshly prepared β-Mo_2C was measured for comparison (**Figure S6**). The polarization curves for β-Mo_2C-0.4 and β-Mo_2C-0.65 overlap each other, suggesting similar HER catalytic properties for samples treated under these two different potential windows. For β-Mo_2C-*x* (*x*=0.75, 0.85, 0.975, and 1.2), the HER current densities decreased at a given potential with the increase of upper limit potential value *x*, indicating the surface oxidation of β-Mo_2C catalysts is detrimental to the HER activity.

We carried out a semi-quantitative analysis of surface oxidation and HER activity relationship based on the CV and the LSV. In our treatment, the degree of surface oxidation is related directly to the total number of electrons withdrawn from the sample surface during the electrochemical oxidation. The total number of oxidation charge (Q_0) was obtained as the integral of current over time, that is, $Q_0 = \int Idt$, where t is the time and I is the total current. Thus, the higher the value of Q_0, the higher the degree of oxidation. Our data indicate the surface of β-Mo_2C-1.2 should be fully oxidized after the treatment, since no oxidative current could be observed at 1.2 V by CV. The fully oxidized nature was also confirmed by the close-to-zero current density after the second and third treatments, monitored by CV (**Figure S7**). The HER polarization curves were further examined by performing Tafel analysis. Tafel slopes (β_T) around the onset potential, *i.e.*, where the current density reached 1 mA/cm^2, were calculated. The obtained values are summarized in **Table 1**.

Table 1. Results of oxidation charge, Tafel slope, and capacitance of oxidized β-Mo_2C electrocatalysts after treatments under different potential windows

U_{max}^* (V)	Q_0 (mC)	β_T ($mV\cdot dec^{-1}$)	C ($mF\cdot cm^{-2}$)
0.4	-0.17±0.04	96.9±0.6	4.39±0.19
0.65	1.9±0.1	103.8±3.3	4.36±0.48
0.75	11.3±0.5	104.4±3.0	3.88±0.36
0.85	19.6±1.5	117.5±2.0	3.04±0.46
0.975	25.2±1.5	150.6±7.2	2.23±0.55
1.2	25.4±1.3	159.3±14.1	2.18±0.41

*: U_{max} is the highest applied oxidative potential for the electrochemical treatment of β-Mo_2C.

Figure 2c shows the Q_0 values as a function of the upper limit potential used for making surface-oxidized samples. Both Q_0 and β_T exhibit an S-shaped curve from 0.4 to 1.2 V. The curvature reaches the maximum for the samples made at the oxidation potential of around 0.8 V. This is consistent with the highest current density, *i.e.*, the fastest reaction rate of surface oxidation, as shown in **Figure 2a**. Since Tafel slope is a kinetic parameter, its increase as a function of surface oxidation suggests either the number of active sites were reduced, or these surface sites deactivated. The experimental data indicates the kinetically sluggish rate-determining step of HER is associated to those oxygen-incorporated surface sites. However, these surface sites were still HER active, since even β-Mo_2C-1.2 exhibited a current density over 10 mA/cm^2 at the potential of -0.5 V. The ECSA value could be estimated based on the analysis of double layer capacitance (*C*) (**Figure 2d** and **Figures S8-S10**). The change of capacitance follows an inverted S-shape and reaches a plateau with the Mo_2C electrode having the highest degree of surface oxidation.

3.3 Spectroscopic study of oxidized β-Mo_2C

X-ray photoelectron spectroscopy was performed to examine the evolution of surface compositions of as-prepared and surface-oxidized β-Mo_2C-*x* electrocatalysts (**Table S2**).[40] All XPS data were analyzed after the calibrations using the adventitious C 1s peak binding energy (BE) value of 284.8 eV. **Figure 3** shows the survey scan, Mo 3d, C 1s, and O 1s for as-prepared β-Mo_2C, β-Mo_2C-0.4, and fully oxidized β-Mo_2C-1.2, respectively. Our XPS survey scan shows the surface of as-prepared β-Mo_2C contains oxygen, molybdenum, and carbon (**Figure 3a**). The oxygen peaks were observed because of the passivation in 2% O_2. Three valence states were identified for Mo based on its 3d XPS peaks: Mo (VI) at 235.9 eV ($3d_{3/2}$) and 233.0 eV ($3d_{5/2}$), Mo (IV) at 232.4 eV ($3d_{3/2}$) and 229.8 eV ($3d_{5/2}$), and Mo (II) at 232.7 eV ($3d_{3/2}$) and 228.8 eV ($3d_{5/2}$) (**Figure 3b**).[40] This result indicates at least three kinds of Mo-based species co-exist in the surface nanostructures, which may include MoO_3, MoO_2, and Mo_2C. The C-Mo bond could be confirmed with the metal carbide peak at 283.4 eV in the C 1s spectrum (**Figure 3c**). In the O 1s region, the O-C peak at 532.0 eV is more intense than the O-Mo peak at 530.6 eV, which could be a result of the carbon support in the sample or a preferable O deposition on carbon-terminated sites rather than Mo-terminated sites in the carbides (**Figure 3d**). Thus, for passivated, as-prepared β-Mo_2C without electrochemical oxidation, there might be exposed metallic sites on the surface. Such samples also had higher HER current density than any of the electrochemically oxidized samples (**Figure S6**). This experimental result is consistent with our computational results that two third of surface Mo sites are predicted to remain exposed (Section 3.4.1). In the survey scan of β-Mo_2C-0.4, the strong F peaks come from Nafion used in the preparation of ink (see Section 2.3) (**Figure 3e**). It appears that Mo (II) peaks of β-Mo_2C-0.4 are much weaker than those of as-prepared β-Mo_2C (**Figure 3f**). Meanwhile, there is no C-Mo peak at 283.4 eV in the C 1s region (**Figure 3c** and **Figure 3g**). Instead, the deconvolution analysis suggests a weak peak centered at 286.7 eV. Such variations in both Mo 3d and C 1s peaks indicate significant changes of surface compositions in these samples. This observation does not mean the new surface sites were deactivated due to further surface oxidation, because the HER activity only got slightly lower for the β-Mo_2C-0.4 sample (**Figure 2b** and **Figure S6**). In addition, in the Mo 3d region of β-Mo_2C-0.4 (**Figure 3f**), the Mo (IV) peak shifted to a lowered energy of 229.3 eV ($3d_{5/2}$), representing a -0.5 V shift in BE, compared with that shown in **Figure 3b**. Such BE change of Mo indicates the valence state is likely between Mo (II) and Mo (IV). Simultaneously, the C 1s XPS peak shifted from 283.4 eV for C-Mo to 286.7 eV for Mo-C-O (**Figure S11**). This structural change could account for the significant change in XPS for β-Mo_2C-0.4 when compared with that of as-prepared β-Mo_2C, despite there being no significant oxidization current in this potential window (**Figure 2a**). The convergent XPS data indicate the surface Mo-C species were mostly converted into Mo-C-O in the Mo_2C electrocatalyst if the oxidation potential reached 0.4 V. However, the as-assigned Mo-C-O peak of β-Mo_2C-x (x=0.4, 0.65, 0.75, and 0.85) shifted towards high energy after the oxidation potential reached 0.975 V (**Figure S11**). A drop in the percentage of peak area coincides with the disappearance of Mo(II) in Mo 3d spectra (**Figure 3j** and **Figure S12n**), indicating a more oxidized surface, such as C-Mo-O moiety as suggested by the DFT calculations. In the O 1s region of β-Mo_2C-0.4, the peak at 534.2 eV is assigned to O-S from Nafion used in the ink (**Figure 3h**). No Mo (II) peaks were detected in the Mo 3d region of β-Mo_2C-1.2, and the observed weak peaks could be assigned to Mo (IV), suggesting this XPS signal may come from the sub-layer Mo atoms (**Figure 3j**). There is no major difference in C 1s XPS peak between β-Mo_2C-1.2 and β-Mo_2C-0.4 (**Figure 3k**). However, the XPS signals from O-C and O-Mo suggest C and Mo react with O differently during the electrochemical oxidation (**Figure 3l**).

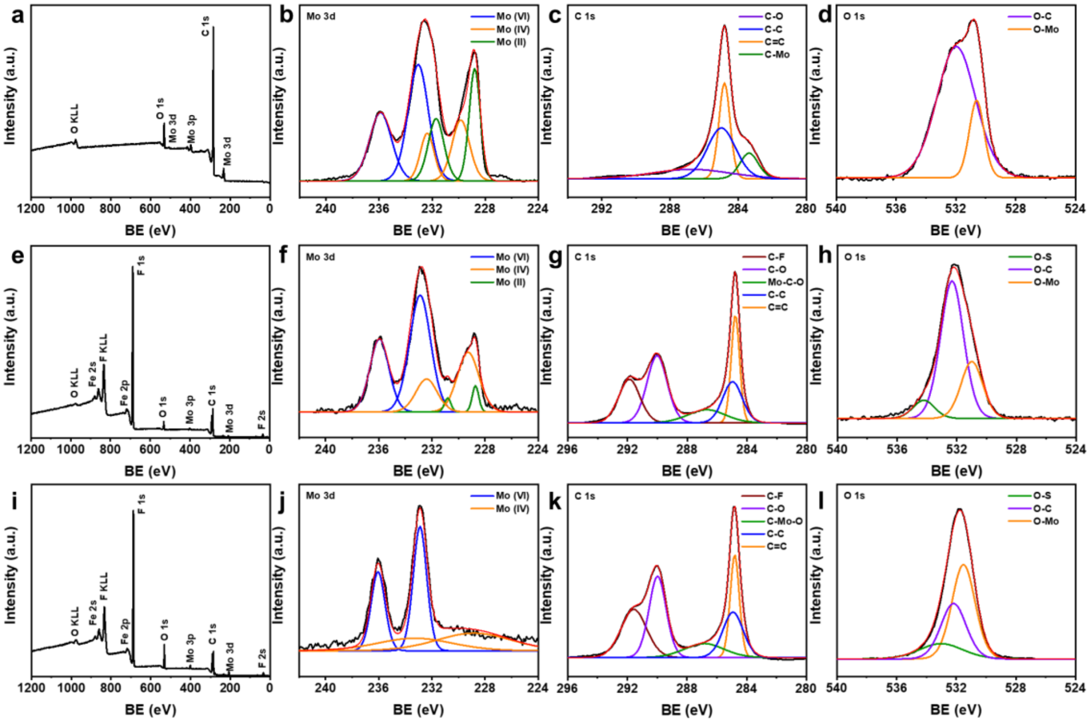

Figure 3. XPS of survey scan, Mo 3d, C 1s, and O 1s for (a-d) as-prepared β-Mo_2C, (e-h) electrochemically partially oxidized β-Mo_2C-0.4, and (i-l) fully oxidized β-Mo_2C-1.2.

Besides the comparative analysis of as-prepared, electrochemically partially oxidized (β-Mo_2C-0.4) and fully oxidized (β-Mo_2C-1.2) samples, we further examined Mo 3d, C 1s, and O 1s XPS spectra for the entire series of oxidized samples to understand the detailed surface compositions after different treatments for surface oxidation. The Mo(II) peaks exist throughout the partially oxidized samples that were created under the oxidative potential lower than or equal to 0.85 V (x=0.4, 0.65, 0.75, and 0.85) (**Figure 4a**). However, the C 1s spectra of these oxidized β-Mo_2C-x do not exhibit the carbide carbon peak at 283.4 eV (**Figure 3g** and **Figure S12**). These spectroscopic data suggest the formation of surface oxycarbide once the oxidation potential reaches 0.4 V. The transition from carbide to oxycarbide can explain the disappearance of carbide C 1s peak of β-Mo_2C-0.4. The strong anodic peak starting at 0.6 V for β-Mo_2C-x (x>0.4) however suggest a further oxidation event that differs from the aforementioned formation of oxycarbide. Experimentally we observed the XPS Mo(II) peaks disappeared for β-Mo_2C-0.975 and β-Mo_2C-1.2, indicating the surface oxycarbide was not stable and further oxidized once the potentials were higher than 0.975 V. Only Mo(IV) and Mo (VI) peaks are observed for β-Mo_2C-0.975 and β-Mo_2C-1.2. The XPS data indicate MoO_3 is the dominant phase for Mo species on the surface for β-Mo_2C-1.2.

The O 1s XPS data provide additional insights into the change of surface structures for these partially oxidized β-Mo_2C, providing information for understanding the interactions between oxygen and surface oxycarbide (**Figure 4b**). For β-Mo_2C-*x* (*x* =0.4, 0.65, 0.75), XPS O 1s spectra show signals from both O-C and O-Mo, suggesting a competitive chemisorptions of oxygen onto surface Mo and C atoms, which is consistent with the existence of surface oxycarbide. When oxidation potential was raised above 0.75 V, the O-Mo peak began to dominate, suggesting the formation of MoO_x. The relative peak intensity in XPS O 1s between O-C and O-Mo decreased at potentials higher than 0.75 V (**Figure S13**), indicating the elimination of CO_x species, which is explained further based on our computational results (Section 3.4.1).

The XPS data, together with the electrochemical results, thus indicate the surface may evolve into oxycarbide first and then into oxide after electrochemical treatments under different potential windows. If oxygen interacted with C-terminated surface (Mo-C), an oxycarbide (Mo-C-O) surface formed. The observation that molybdenum oxycarbide (Mo-C-O) fragments in the XPS C 1s region for all oxidized samples indicates this formation pathway (**Figure 3c**, **3g**, **3k** and **Figure S12**). For Mo-terminated surfaces (C-Mo), XPS data suggest Mo-O surface formed as the limit of forward potential increased. The intensity of O-Mo peak in O 1s XPS of β-Mo_2C-*x* grew when the *x* value changed from 0.75, to 0.85, 0.975, and 1.2, indicating the continuing formation of surface Mo-O species.

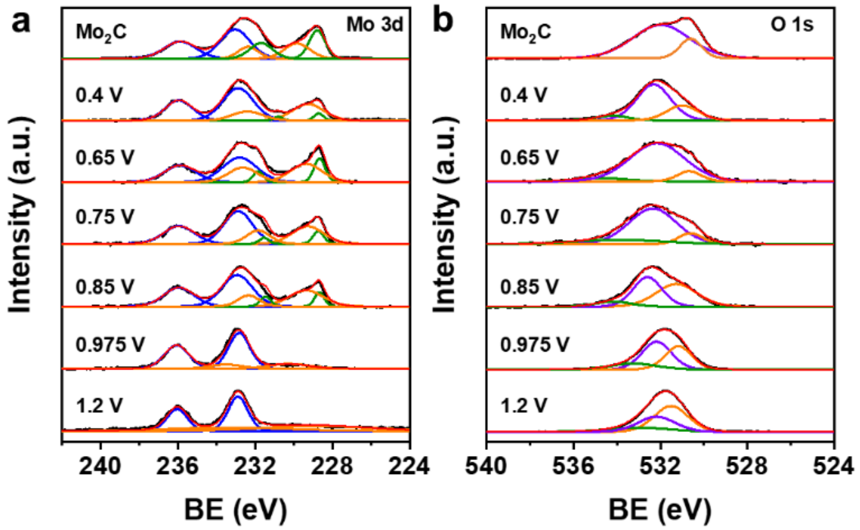

Figure 4. XPS of β-Mo_2C electrocatalysts in (a) Mo 3d (violet: VI; orange: IV; green: II) and (b) O 1s (green: O-S; violet: O-C; orange: O-Mo) regions, exhibiting evolution of surface compositions as a function of the upper limit of potential used in the electrochemical oxidation process.

3.4 DFT and *ab initio* thermodynamic calculations

3.4.1 Evolution of surface motifs during electrochemical oxidation of β-Mo_2C

Theoretical calculations were carried out to gain insights into the change of atomic structures of Mo_2C surface after the electrochemical oxidative treatments. **Figure 5** shows the O* surface configurations that are most thermodynamically stable in the potential range of 0 to 0.6 V, along with their free energies. In the range of 0 to 0.28 V, the model predicts the partially oxidized surface to be the most stable, with 1/3 of hollow Mo sites and all exposed C sites covered with O*, denoted as $(Mo\text{-}O)_1(C\text{-}O)_6$. In this potential window, 2/3 of Mo sites are predicted to remain exposed. Less oxidized surfaces (*i.e.*, $(Mo\text{-}O)_0(C\text{-}O)_n$, n=1~6) are found to be less thermodynamically stable by more than 1 eV and thus expected not to form at any positive potentials (**Figure 5b**). The lowest (most negative) lines correspond to the most stable surfaces at specific potential windows, marked by colored regions. Two hatched regions depict the slow and fast CO/CO_2 removal, respectively, which leads to the C* substitution with O* and the formation of surface oxide. Our simulation indicates the increase in the applied potential results in further oxidized structures $(Mo\text{-}O)_3(C\text{-}O)_6$ and $(Mo\text{-}O)_4(C\text{-}O)_6$, which first appear at 0.28 and 0.51 V, respectively. In $(Mo\text{-}O)_3(C\text{-}O)_6$, all Mo and C sites are covered with O*, whereas in $(Mo\text{-}O)_4(C\text{-}O)_6$, an extra oxygen atom brings about surface restructuring through the displacement of C-O. The formation of oxidized surfaces at low potentials is consistent with C 1s XPS spectrum of β-Mo_2C-0.4, which exhibits both C-O and Mo-C-O oxycarbide features (**Figure 3e-h**). **Table 2** shows the average Mo oxidation states obtained from calibrated Bader charges (**Figure S1**). For partially oxidized $(Mo\text{-}O)_n(C\text{-}O)_6$ structures, the Mo oxidation states are close to +2, which corresponds to Mo(II) peaks in XPS data for β-Mo_2C and β-Mo_2C-0.4 (**Figure 3b** and **3f**).

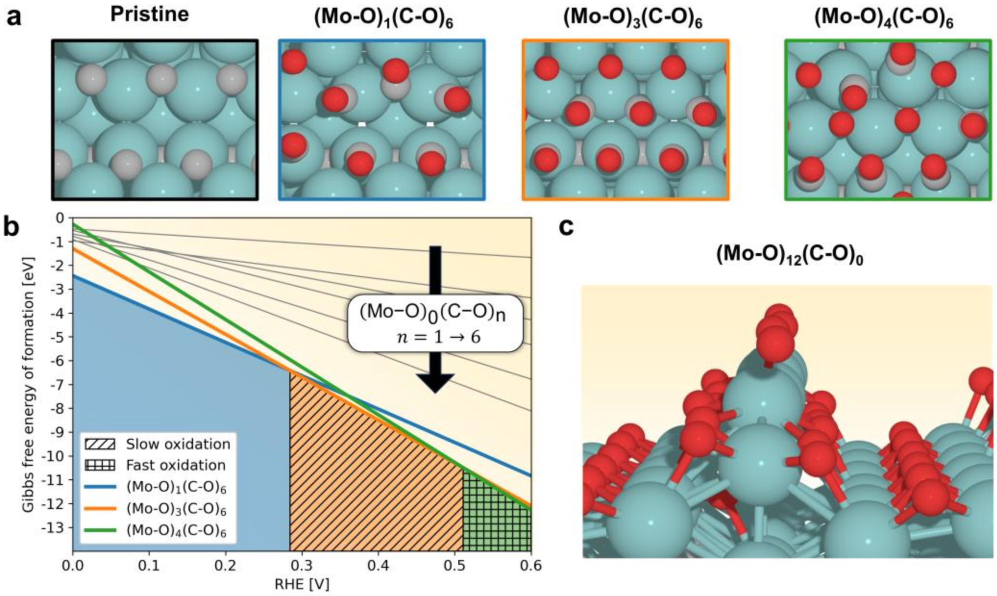

Figure 5. Thermodynamically stable β-Mo_2C(011) C-terminated surfaces in the potential range of 0 to 0.6 V. (a) Top view of identified structures. Pristine surface is included for reference. (b) Gibbs free energy of formation as a function of applied potential. (c) Proposed surface oxide structure formed after the complete oxidation in hatched regions at a higher potential (cyan: Mo; grey: C; red: O).

Table 2. Average and calibrated Bader charges on surface Mo atoms

Surface	Net atomic Bader charge	Oxidation state
Pristine β-$Mo_2C(011)$-C	+0.83	+2.21
$(Mo\text{-}O)_1(C\text{-}O)_6$	+0.71	+1.91
$(Mo\text{-}O)_3(C\text{-}O)_6$	+0.81	+2.16
$(Mo\text{-}O)_4(C\text{-}O)_6$	+0.81	+2.16
$(Mo\text{-}O)_{12}(C\text{-}O)_0$	+1.37	+3.57

The measured Q_0 (the total oxidation charge) values due to the formation of an oxidized surface are consistent with and explained by the computational results (**Table 3** and **Equation S12**). The experimentally determined Q_0 values are closely associated with the change of surface species from $(Mo\text{-}O)_1(C\text{-}O)_6$ to $(Mo\text{-}O)_3(C\text{-}O)_6$ and $(Mo\text{-}O)_3(C\text{-}O)_6$ to $(Mo\text{-}O)_4(C\text{-}O)_6$, which occur at 0.28 and 0.51 V, respectively, based on the simulation results. The simulated Q_0 values associated with these changes are found to be 1.31 mC at 0.28 V and 0.65 mC at 0.51 V, which are comparable in magnitude to the experimentally obtained values of -0.17±0.04 mC at 0.4 V and 1.9±0.1 mC at 0.65 V (**Table 1**). The observation that the measured Q_0 at 0.4 V is smaller in magnitude than the predicted one might be due to one of the following factors. The surface after passivation is more oxidized than $(Mo\text{-}O)_1(C\text{-}O)_6$ and stable at a more positive potential due to the sluggish kinetics for the H_2O/O^* adsorption equilibrium over the timescale of CV measurement. Alternatively, the H_2O/O^* equilibrium may be a kinetically fast step, leading to the fully reversible O* surface deposition. In this scenario, the experimental Q_0 reflects an irreversible oxidation of surface oxycarbide to surface oxide. Further studies discussed below suggest that the irreversible oxidation does not occur to a significant degree below 0.5 V, making it more likely for Q_0 to be reflective of irreversible surface oxide formation.

Table 3. Estimates of charge transfer values for surface oxidation

Oxidation step	Charge transfer (mC)
$(Mo\text{-}O)_1(C\text{-}O)_6 \rightarrow (Mo\text{-}O)_3(C\text{-}O)_6$	1.31
$(Mo\text{-}O)_3(C\text{-}O)_6 \rightarrow (Mo\text{-}O)_4(C\text{-}O)_6$	0.65
$(Mo\text{-}O)_1(C\text{-}O)_6 \rightarrow (Mo\text{-}O)_{12}(C\text{-}O)_0$	7.19

Replace all C in a nanoparticle to O	45.2

As the $(Mo\text{-}O)_4(C\text{-}O)_6$ species is predicted to form at 0.51 V, no more exposed surface Mo and C sites are available for reaction with O* following the previously suggested pathway. Thus, the experimentally observed high oxidation currents at potentials above 0.5-0.6 V should come from other sources, namely, the subsurface structures having higher oxygen coverages may involve C* substitution with H_2O-derived O*. In such a process, surface carbon may react and form CO and CO_2 species, which subsequently leave the surface. This surface reaction should result in the formation of vacancies that are filled with oxygen atoms and, as a result, two electrons (along with two H^+) are released per every substituted carbon atom. Indeed, computationally we found that C* substitution for O* is thermodynamically favorable at a wide range of applied positive potentials from 0.05 V to 1.2 V (**Note S3**).

Our simulation results further indicate that the computed energy barrier for CO removal is a suitable parameter to evaluate the kinetic stability of oxidized surfaces. The removal of CO is proposed to be the rate-limiting step (RLS) in substitutive oxidation, as the follow-up reoxidation of highly oxophilic vacancies is expected to be fast. **Table 4** summarizes the calculated values of kinetic barriers for CO and CO_2 removals on the relevant Mo-C surfaces, agreeing with the substitutive oxidation process at high O* coverages. The HSE level of theory calculation reveals CO desorption to be more favorable than CO_2 formation and shows high energy barriers for low-coverage surfaces: 1.79 eV for $(Mo\text{-}O)_0(C\text{-}O)_6$ and 1.61 eV for $(Mo\text{-}O)_1(C\text{-}O)_6$ structures, suggesting good kinetic stability. This result is consistent with the predicted lack of a significant current in the relevant thermodynamic stability window of $(Mo\text{-}O)_1(C\text{-}O)_6$ (0-0.28 V, **Figure 5b**). The $(Mo\text{-}O)_3(C\text{-}O)_6$ structure which is thermodynamically stable within 0.28-0.51 V exhibits a moderate barrier of 0.71 eV and is predicted to undergo substitutive oxidation. In contrast, the CO removal barrier for $(Mo\text{-}O)_4(C\text{-}O)_6$ which is thermodynamically stable above 0.51 V is found to be very low (0.07 eV or less), indicating that this structure is kinetically unstable and shall rapidly lose CO, resulting in C* substitution with O*, leading to the transformation from metal oxycarbide to oxide on the surface.

Table 4. Kinetic barriers for CO and CO_2 removal computed at the HSE level of theory*

Surface	CO (eV)	CO_2 (eV)
$(Mo\text{-}O)_0(C\text{-}O)_6$	1.79 (1.98)	2.58 (2.44)
$(Mo\text{-}O)_1(C\text{-}O)_6$	1.61 (1.18)	2.75 (2.34)
$(Mo\text{-}O)_3(C\text{-}O)_6$ type-1	0.73 (0.84)	1.05 (1.11)
$(Mo\text{-}O)_3(C\text{-}O)_6$ type-2	0.71 (0.83)	1.37 (1.53)
$(Mo\text{-}O)_4(C\text{-}O)_6$	0.0** (0.07)	0.07 (0.07)

*: Values in parentheses are obtained using the PBE functional.

**: Energy difference came out negative (-0.0071 eV) and thus represented as zero.

Our simulation data also suggest that CO* desorption is no longer the RLS of the "substitutive" oxidation when the applied potential is above 0.51 V. The corresponding energy barrier on $(Mo\text{-}O)_4(C\text{-}O)_6$ at 0.51 V is very low and should yield currents much greater than those observed in the experiment (**Table S3**). At these potentials, the reaction kinetics is likely limited by the formation of H_2O-dervied O*. Our simulation data suggest H_2O binds weaker to more oxidized surfaces, which shall destabilize the transition states for breaking the O-H bond. For example, the adsorption energy of H_2O changes from -1.06 eV on the exposed Mo atoms of pristine β-$Mo_2C(011)$-C to -0.1 eV on $(Mo\text{-}O)_2(C\text{-}O)_6$ and +0.19 eV on $(Mo\text{-}O)_3(C\text{-}O)_6$, reflecting weak hydrogen bonding and unavailable sites of Mo (**Table S4**). Water dissociation, accelerated by the potential,[68] is likely responsible for the 0.1 V shift of the onset potential (0.6 V) from the predicted value (0.51 V) of the oxidation current and attributed to the exponentially rising oxidation current above 0.6 V. It should be noted that lowered onsets of oxidation potential can be obtained in principle. Such reduction in onset potential requires thermodynamic equilibria among $(Mo\text{-}O)_n(C\text{-}O)_6$ structures that lie closely in energy (**Figure 5b**) and a two-step process where the surface is first oxidized, followed by CO* desorption. For example, less oxidized $(Mo\text{-}O)_1(C\text{-}O)_6$ can undergo substitutive oxidation at potentials as low as ~0.25 V, since kinetically unstable $(Mo\text{-}O)_4(C\text{-}O)_6$ is only 0.62 eV greater in free energy, resulting in an effective energy barrier of 0.71 eV for the removal of CO. The energy barrier is low enough for the two-step oxidation process to take place on the time scale of tens of seconds, suggesting an exponential increase in current density at potentials above 0.25 V, due to the potential dependence of $(Mo\text{-}O)_4(C\text{-}O)_6$ formation. This predicted reaction pathway however was not experimentally observed, and the sluggish H_2O dissociation (*vide supra*) likely limits the further oxidation of $(Mo\text{-}O)_3(C\text{-}O)_6$.

We thus categorize the CO*-desorption and H_2O*-dissociation limited oxidation pathways as the slow and fast substitutive oxidations, respectively (the hatched regions in **Figure 5b**). After it is formed at 0.28 V, $(Mo\text{-}O)_3(C\text{-}O)_6$ experiences slow substitutive oxidation governed by the removal of CO*. At 0.51 V, the formation of kinetically unstable $(Mo\text{-}O)_4(C\text{-}O)_6$ becomes thermodynamically favorable, which corresponds to fast substitutive oxidation, limited by H_2O dissociation. The slow substitutive oxidation of the $(Mo\text{-}O)_3(C\text{-}O)_6$ surface should result in the decrease of Mo(II) peaks for the β-Mo_2C-0.4 V sample (**Figure 3b** and **3f**). To determine the Mo oxidation state after its substitutive oxidation, we investigated the limiting $(Mo\text{-}O)_{12}(C\text{-}O)_0$ structure shown in **Figure 5c**. Unlike $(Mo\text{-}O)_3(C\text{-}O)_6$, in which Mo coordinates to Mo, C, and O and adopts +2 oxidation state, the surface Mo in $(Mo\text{-}O)_{12}(C\text{-}O)_0$ is only coordinated to O, adopting +3.57 oxidation state and a distorted octahedral geometry (Mo(IV)) (**Figure 6**). Our computational results suggest that the substitutive oxidation results in a progressive change in the Mo oxidation state and chemical environment, which agrees very well with the experimentally observed potential-dependent current density changes that correspond to the surface transformation from metal oxycarbide to oxide. Experimentally, XPS data show a reduced peak area in the Mo(II) region and an increase in Mo(IV) (**Figures 3 and 4**).

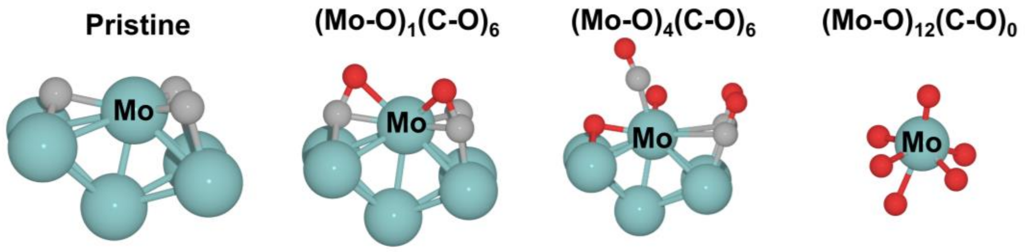

Figure 6. Illustrations of nearest neighboring atoms for a given Mo at different surface coverages.

Compared with computational results based on the substitutional oxidation (**Table S3**), the experimentally observed current densities are low for samples made after oxidative treatment below 0.6 V. Our computational and experimental results suggest that two effects might be at play. First, CO* species may be removed and replaced with O* during the passivation step. A large extent of pre-oxidation is supported by the Q_0 "total oxidation" value of 25.4 mC (**Table 1**), being less than that required to convert the pristine Mo_2C completely to MoO_2 (~45.2 mC), and by the XPS data (**Figure 3**). Second, CO* may be protonated and exist in the form of COH* at low potentials, preventing the desorption of CO. Computationally, we found a partially hydroxylated $(Mo\text{-}OH)_3(C\text{-}OH)_4(C\text{-}O)_1+H_2O^*$ surface to be very stable thermodynamically across a wide range of potentials up to 0.31 V (**Figure 7**). From the comparison of free energies of $(Mo\text{-}O)_3(C\text{-}O)_6$ and $(Mo\text{-}OH)_3(C\text{-}OH)_6$ surfaces at 0 V, we expect that deprotonation on average should increase the effective desorption energy of CO by ~ 0.2 eV. This energy barrier should result in reducing the current density down to ~0.1 mA/cm^2, in line with the observed experimental results. Thus, substitutive oxidation should be minor when the potential window for the treatment is below 0.5 V.

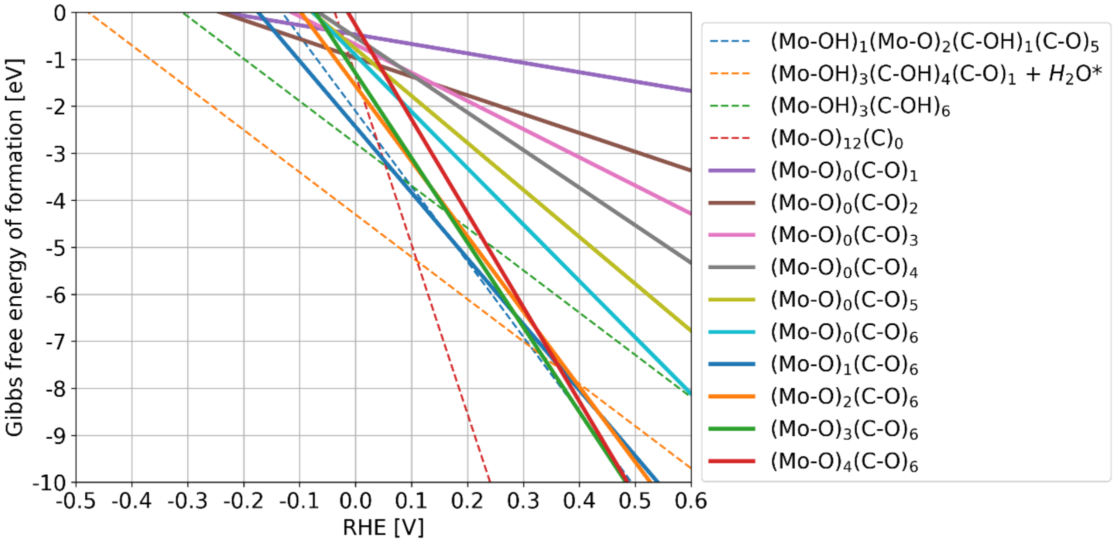

Figure 7. Gibbs free energy of formation of a range of Mo- and C-containing structures. Solid lines represent energies of $(Mo\text{-}O)_n(C\text{-}O)_m$ structures where n=0~4 and m=1~6. Dashed lines denote four relevant, special cases of hydroxylated and fully oxidized surfaces.

3.4.2 Theoretical analysis of HER catalyzed by partially oxidized β-Mo_2C

The surface oxides formed after substitutive oxidation at above 0.6 V (**Figure 5c**) should be stable at negative potential ranges, since this electrochemical treatment is irreversible due to the release of gaseous species such as CO and CO_2. This predicted change is consistent with the experimental results, which exhibit no reduction peak during the backward CV scan (**Figure 2a**). The polarization curves for HER measurement are relatively stable after 30 cycles of CV scans in the range of 0~-0.5 V (*vs.* RHE) (**Figure S14**). **Table 2** reports the existence of Mo(IV) in the limiting structure of $(Mo\text{-}O)_{12}(C\text{-}O)_0$, which corresponds to surface MoO_2. As MoO_2 and MoO_3 exhibit much lower HER activity in comparison with β-Mo_2C,[74, 75] the substitutive oxidation leading to the surface oxide should deactivate the carbide surface. Interestingly, β-Mo_2C-1.2 exhibited HER currents closely matching those of MoO_2/MoO_3,[74, 75] indicating a complete surface oxidation to MoO_x and the absence of (oxy)carbide features. Higher HER activities observed on less oxidized surfaces ($x<1$, **Figure 2b**) indicate incomplete substitutive oxidation of the surface, and the likely existence of oxycarbide structural motifs that catalyze the HER. Since the charge required to form a surface oxide layer is 7.19 mC, which is less than that of 11.3 mC for U_{max} of 0.75 V and 19.6 mC for 0.85 V, and the HER activity is still significant, bulk oxidation involving subsurface carbons may occur under these conditions.

Unlike the substitutive oxidation, the additive oxidation associated with O* chemisorption below 0.5 V that leads to $(Mo\text{-}O)_n(C\text{-}O)_m$ structures is reversible (**Figure 5b**). Indeed, an Eley-Rideal-type process is feasible, in which O* is protonated to form OH* and then H_2O* at more negative potentials, followed by the desorption of water molecule. The computationally predicted reversibility is consistent with the lack of hysteresis on CV in the potential window of 0-0.4 V (**Figure 2a**). It also explains the similarity in HER activity between as-prepared β-Mo_2C and β-Mo_2C-0.4 (**Figure 2b**). Thus, both $(Mo\text{-}O)_1(C\text{-}O)_6$ and $(Mo\text{-}O)_3(C\text{-}O)_6$ surfaces, predicted to form below 0.28 and 0.51 V, respectively, likely undergo further conversion during HER at negative U to the same catalytically active surface.

Our thermodynamic calculations also shed light on the state of surface at negative potentials. Without protonation, $(Mo\text{-}O)_1(C\text{-}O)_6$ structure which is stable at U of 0 V loses some oxygen to form $(Mo\text{-}O)_0(C\text{-}O)_2$ below -0.15 V (**Figure 7**). With protonation, O* reacts with proton-electron pairs to form OH*. This process stabilizes greatly chemisorbed oxygen, forming a surface with mixed OH* and H_2O* at the reducing potentials (**Figure 7**). The H_2O-absorbed $(Mo\text{-}OH)_3(C\text{-}OH)_4(C\text{-}O)_1$ configuration is particularly stable. The Mo-bound H* is likely present as well (*vide infra*). All such species are expected to be further stabilized through hydrogen bonding. Formation of oxygen vacancy is likely inhibited, and the surface remains stable during the anodic electrochemical treatment of the catalyst.

We further analyzed the nature of active site towards HER once the hydroxylated surface is formed at a negative potential. Under such conditions, HER is expected to occur on the sites of Mo*/C-O* pairs. Water dissociation on a neighboring Mo site coupled with an H diffusion from a neighboring C-OH* yields a stable Mo-H*/C-OH* intermediate, followed by the removal of H_2. In this mechanism, H_2 release is expected to be facile, since its transition state is stabilized through the interaction with a frustrated Lewis acid/base pair of Mo*-O*, and Mo and O are oppositely charged. A similar mechanism in the reverse process (H_2 dissociation) has been proposed on metal oxide surfaces.[76, 77] As the formation free energies of H_2O-derived intermediates on Mo sites rank as H*<H_2O*<OH*<O* at 0 V, corresponding to ΔG of -1.12, -1.06, -0.64, and -0.47 eV, respectively, on a pristine surface, we anticipate that surface Mo-OH* motifs recombine to form weakly bound H_2O* which is then replaced by H* (**Table S5**). Thus, the formation of Mo-H*/C-OH* is expected to be thermodynamically favorable.

4. Conclusion

In this study, we semi-quantitively elucidated the important effects of surface oxidation of β-Mo_2C electrocatalyst on HER. We achieved a varied degree of surface oxidization using an electrochemical treatment operated under different potential windows. The convergent experimental and computational data point to a reaction pathway in which surface oxidation occurs through C first and then Mo oxidations when the upper limit of the potential window increases. There is also a good agreement between theory and experiment on the exposed sites and their activities for partially or fully oxidized Mo_2C electrocatalysts. Specifically, XPS data suggest the formation of surface oxycarbide due to the incorporation of oxygen to carbide-terminated surface sites at low potentials (~0.4 V) and the formation of surface Mo(VI) oxide at the final state. Tafel slope and double-layer capacitance analyses indicate a relationship surface oxidization should negatively affect the HER performance.

Computationally, DFT and *ab initio* thermodynamic calculations unveil substantial amounts of H_2O-derived oxygen on all electrochemically treated surfaces of β-Mo_2C electrocatalysts. Two mechanisms dominate the surface oxidation in the electrochemical processes: a reversible additive oxidation through O* chemisorption (<0.51 V) and an irreversible substitutive C*-to-O* oxidation with the concomitant loss of CO (>0.51 V). The substitutive oxidation is associated with a pronounced anodic current at 0.6 V, the formation of a Mo(IV) surface oxide, and a subsequent decline in the HER activity at negative potentials. The additive oxidation yields Mo(II) oxycarbide structures that expose C=O groups and readily react with proton-electron pairs. Protonation favors the surface oxidation and is expected to stabilize the surface against the loss of gaseous oxidative C species. Surface hydroxyls readily recombine and expose Mo*/C-O*, which are proposed to function as frustrated Lewis acid/base pairs and catalyze HER. This work helps to unravel the effect of surface oxidation on catalytic properties and paves the way for developing practical use of molybdenum carbides in a range of reactions.

Supporting information

Micrographs, cyclic voltammetry curves, polarization curves, capacitance measurement, XPS data and analysis, notes for DFT and *ab initio* thermodynamic calculations can be found in the Supporting Information file.

Author contributions

S. Y. conceptualization, methodology, writing – original draft, writing - review & editing, data curation, validation, analysis. **A. G.** data curation, writing – original draft, writing - review & editing. **D. G.** conceptualization, methodology, data curation **A. N. K.** data curation. **H. H.** data curation. **A. M.** supervision, conceptualization, methodology, investigation, resources, funding acquisition, writing – original draft, writing - review & editing. **H. Y.** supervision, conceptualization, investigation, resources, funding acquisition, writing - review & editing.

Conflicts of interest

The authors declare no competing financial interest.

Acknowledgements

This work is supported in part by the National Science Foundation (CBET-2055734 to HY and DMREF-2323988 to AM), and University of Illinois Urbana-Champaign (UIUC). Electron microscopy characterizations and X-ray photoelectron spectroscopy were carried out at the Frederick Seitz Materials Research Laboratory Central Research Facilities, UIUC. The X-ray diffraction was carried out at the George L. Clark X-ray Facility and 3M Materials Laboratory, School of Chemical Science (SCS) at UIUC. S. Y. is grateful for a Chia-Chen Chu Fellowship from the SCS.

Notes and references

1. X. Zhang, C. Shi, B. Chen, A. N. Kuhn, D. Ma and H. Yang, *Curr. Opin. Chem. Eng.*, 2018, **20**, 68-77.
2. S. Sun, Y. Liu, G. Xu, C. Jiang, J. Li, L. Fan and W. Cai, *Fuel*, 2023, **335**, 127084.
3. Z. Zhou, Y. Jia, Q. Wang, Z. Jiang, J. Xiao and L. Guo, *Sustainability*, 2023, **15**, 14556.
4. B. Izelaar, D. Ripepi, S. Asperti, A. I. Dugulan, R. W. A. Hendrikx, A. J. Böttger, F. M. Mulder and R. Kortlever, *ACS Catal.*, 2023, **13**, 1649-1661.
5. R. Zhao, Y. Chen, H. Xiang, Y. Guan, C. Yang, Q. Zhang, Y. Li, Y. Cong and X. Li, *ACS Appl. Mater. Interfaces*, 2023, **15**, 6797-6806.
6. S. Zhang, J. Wang, L. Ye, S. Li, Y. Su and H. Zhang, *Chem. Eng. J.*, 2023, **454**, 140072.
7. J. Pang, J. Sun, M. Zheng, H. Li, Y. Wang and T. Zhang, *Appl. Catal., B*, 2019, **254**, 510-522.
8. J. R. Kitchin, J. K. Nørskov, M. A. Barteau and J. G. Chen, *Catal. Today*, 2005, **105**, 66-73.
9. Q. Gong, Y. Wang, Q. Hu, J. Zhou, R. Feng, P. N. Duchesne, P. Zhang, F. Chen, N. Han, Y. Li, C. Jin, Y. Li and S.-T. Lee, *Nat. Commun.*, 2016, **7**, 13216.
10. L. G. Hernández-Maya, I. Zapata-Peñasco, M. Olivares-Luna, I. Campos-Silva, J. Martínez-Trinidad, L. G. Díaz-Barriga, J. N. Rivera-Olvera and V. Garibay-Febles, *Surf. Coat. Technol.*, 2023, **469**, 129816.
11. J. Xu, Z. Li, S. Xu, P. Munroe and Z.-H. Xie, *J. Power Sources*, 2015, **297**, 359-369.
12. C. Wan, Y. N. Regmi and B. M. Leonard, *Angew. Chem. Int. Ed.*, 2014, **53**, 6407-6410.
13. C. Tang, H. Zhang, K. Xu, Q. Zhang, J. Liu, C. He, L. Fan and T. Asefa, *J. Mater. Chem. A*, 2019, **7**, 18030-18038.
14. H. Lin, Z. Shi, S. He, X. Yu, S. Wang, Q. Gao and Y. Tang, *Chem. Sci.*, 2016, **7**, 3399-3405.
15. X. Zhang, J. Wang, T. Guo, T. Liu, Z. Wu, L. Cavallo, Z. Cao and D. Wang, *Appl. Catal., B*, 2019, **247**, 78-85.
16. P. Yin, H. Cai, X. Zhang, B. Chen, Y. Liu, R. Gao and C. Shi, *New J. Chem.*, 2021, **45**, 10396-10401.
17. L. Lin, W. Zhou, R. Gao, S. Yao, X. Zhang, W. Xu, S. Zheng, Z. Jiang, Q. Yu, Y.-W. Li, C. Shi, X.-D. Wen and D. Ma, *Nature*, 2017, **544**, 80-83.
18. S. Yao, X. Zhang, W. Zhou, R. Gao, W. Xu, Y. Ye, L. Lin, X. Wen, P. Liu, B. Chen, E. Crumlin, J. Guo, Z. Zuo, W. Li, J. Xie, L. Lu, C. J. Kiely, L. Gu, C. Shi, J. A. Rodriguez and D. Ma, *Science*, 2017, **357**, 389-393.
19. X. Zhang, M. Zhang, Y. Deng, M. Xu, L. Artiglia, W. Wen, R. Gao, B. Chen, S. Yao, X. Zhang, M. Peng, J. Yan, A. Li, Z. Jiang, X. Gao, S. Cao, C. Yang, A. J. Kropf, J. Shi, J. Xie, M. Bi, J. A. van Bokhoven, Y.-W. Li, X. Wen, M. Flytzani-Stephanopoulos, C. Shi, W. Zhou and D. Ma, *Nature*, 2021, **589**, 396-401.
20. Z. Li, Z. Qi, S. Wang, T. Ma, L. Zhou, Z. Wu, X. Luan, F.-Y. Lin, M. Chen, J. T. Miller, H. Xin, W. Huang and Y. Wu, *Nano Lett.*, 2019, **19**, 5102-5108.

21. D. A. Kuznetsov, Z. Chen, P. V. Kumar, A. Tsoukalou, A. Kierzkowska, P. M. Abdala, O. V. Safonova, A. Fedorov and C. R. Müller, *J. Am. Chem. Soc.*, 2019, **141**, 17809-17816.
22. G.-Q. Yu, B.-Y. Huang, X. Chen, D. Wang, F. Zheng and X.-B. Li, *J. Phys. Chem. C*, 2019, **123**, 21878-21887.
23. L. Zhao, H. Yuan, D. Sun, J. Jia, J. Yu, X. Zhang, X. Liu, H. Liu and W. Zhou, *Nano Energy*, 2020, **77**, 105056.
24. X. Yang, J. Cheng, X. Yang, Y. Xu, W. Sun and J. Zhou, *Chem. Eng. J.*, 2023, **451**, 138977.
25. C. Yang, R. Zhao, H. Xiang, J. Wu, W. Zhong, X. Li and Q. Zhang, *Nano Energy*, 2022, **98**, 107232.
26. M. M. Sullivan and A. Bhan, *J. Catal.*, 2016, **344**, 53-58.
27. M. M. Sullivan, J. T. Held and A. Bhan, *J. Catal.*, 2015, **326**, 82-91.
28. M. M. Sullivan and A. Bhan, *J. Catal.*, 2018, **357**, 195-205.
29. A. Kumar and A. Bhan, *Chem. Eng. Sci.*, 2019, **197**, 371-378.
30. E. A. Blekkan, C. Pham-Huu, M. J. Ledoux and J. Guille, *Ind. Eng. Chem. Res.*, 1994, **33**, 1657-1664.
31. K. Murugappan, E. M. Anderson, D. Teschner, T. E. Jones, K. Skorupska and Y. Román-Leshkov, *Nat. Catal.*, 2018, **1**, 960-967.
32. A. N. Kuhn, R. C. Park, S. Yu, D. Gao, C. Zhang, Y. Zhang and H. Yang, *Carbon Future*, 2024, **1**, 9200011.
33. J. A. Schaidle, J. Blackburn, C. A. Farberow, C. Nash, K. X. Steirer, J. Clark, D. J. Robichaud and D. A. Ruddy, *ACS Catal.*, 2016, **6**, 1181-1197.
34. B. Zhang, J. Zhou, S. R. Elliott and Z. Sun, *J. Mater. Chem. A*, 2020, **8**, 23947-23954.
35. H. Cheng, L.-X. Ding, G.-F. Chen, L. Zhang, J. Xue and H. Wang, *Adv. Mater.*, 2018, **30**, 1803694.
36. Q. Li, S. Qiu, L. He, X. Zhang and C. Sun, *Phys. Chem. Chem. Phys.*, 2018, **20**, 23338-23343.
37. X. Qu, L. Shen, Y. Mao, J. Lin, Y. Li, G. Li, Y. Zhang, Y. Jiang and S. Sun, *ACS Appl. Mater. Interfaces*, 2019, **11**, 31869-31877.
38. X. Du, R. Zhang, D. Li, C. Hu and H. Garcia, *J. Energy Chem.*, 2022, **73**, 68-87.
39. E. C. Weigert, D. V. Esposito and J. G. Chen, *J. Power Sources*, 2009, **193**, 501-506.
40. J. F. Moulder, W. F. Stickle, P. E. Sobol and K. D. Bomben, *Handbook of X-Ray Photoelectron Spectroscopy*, Perkin-Elmer Corporation, United States of America, 1992.
41. G. Kresse and J. Furthmüller, *Comput. Mater. Sci.*, 1996, **6**, 15-50.
42. G. Kresse and J. Furthmüller, *Phys. Rev. B*, 1996, **54**, 11169-11186.
43. G. Kresse and J. Hafner, *Phys. Rev. B*, 1994, **49**, 14251-14269.
44. G. Kresse and J. Hafner, *Phys. Rev. B*, 1993, **47**, 558-561.
45. G. Kresse and D. Joubert, *Phys. Rev. B*, 1999, **59**, 1758-1775.
46. P. E. Blöchl, *Phys. Rev. B*, 1994, **50**, 17953-17979.
47. J. P. Perdew, K. Burke and M. Ernzerhof, *Phys. Rev. Lett.*, 1996, **77**, 3865-3868.
48. S. Grimme, J. Antony, S. Ehrlich and H. Krieg, *J. Chem. Phys.*, 2010, **132**, 154104.

49. A. V. Krukau, O. A. Vydrov, A. F. Izmaylov and G. E. Scuseria, *J. Chem. Phys.*, 2006, **125**, 224106.
50. Github, The D3 dispersion model, https://github.com/dftd3/simple-dftd3/.
51. H. J. Monkhorst and J. D. Pack, *Phys. Rev. B*, 1976, **13**, 5188-5192.
52. A. Shrestha, X. Gao, J. C. Hicks and C. Paolucci, *Chem. Mater.*, 2021, **33**, 4606-4620.
53. R. J. Fries and C. P. Kempter, *Anal. Chem.*, 1960, **32**, 1898-1898.
54. S. P. Ong, W. D. Richards, A. Jain, G. Hautier, M. Kocher, S. Cholia, D. Gunter, V. L. Chevrier, K. A. Persson and G. Ceder, *Comput. Mater. Sci.*, 2013, **68**, 314-319.
55. W. Sun and G. Ceder, *Surf. Sci.*, 2013, **617**, 53-59.
56. R. F. Ribeiro, A. V. Marenich, C. J. Cramer and D. G. Truhlar, *Phys. Chem. B*, 2011, **115**, 14556-14562.
57. A. Hjorth Larsen, J. Jørgen Mortensen, J. Blomqvist, I. E. Castelli, R. Christensen, M. Dułak, J. Friis, M. N. Groves, B. Hammer, C. Hargus, E. D. Hermes, P. C. Jennings, P. Bjerre Jensen, J. Kermode, J. R. Kitchin, E. Leonhard Kolsbjerg, J. Kubal, K. Kaasbjerg, S. Lysgaard, J. Bergmann Maronsson, T. Maxson, T. Olsen, L. Pastewka, A. Peterson, C. Rostgaard, J. Schiøtz, O. Schütt, M. Strange, K. S. Thygesen, T. Vegge, L. Vilhelmsen, M. Walter, Z. Zeng and K. W. Jacobsen, *J. Phys.: Condens.Matter*, 2017, **29**, 273002.
58. G. Henkelman, B. P. Uberuaga and H. Jónsson, *J. Chem. Phys.*, 2000, **113**, 9901-9904.
59. G. Henkelman and H. Jónsson, *J. Chem. Phys.*, 1999, **111**, 7010-7022.
60. K. Mathew, V. Kolluru, S. Mula, S. N. Steinmann and R. G. Hennig, *J. Chem. Phys.*, 2019, **151**, 234101.
61. K. Mathew, R. Sundararaman, K. Letchworth-Weaver, T. A. Arias and R. G. Hennig, *J. Chem. Phys.*, 2014, **140**, 084106.
62. K. Mathew, Rhennig and J. Bértoli, VASPsol: VASPsol Solvation Module V1.0, https://doi.org/10.5281/zenodo.2555053.
63. W. Tang, E. Sanville and G. Henkelman, *J. Phys.: Condens.Matter*, 2009, **21**, 084204.
64. M. Yu and D. R. Trinkle, *J. Chem. Phys.*, 2011, **134**, 064111.
65. G. Henkelman, A. Arnaldsson and H. Jónsson, *Comput. Mater. Sci.*, 2006, **36**, 354-360.
66. K. Reuter and M. Scheffler, *Phys. Rev. B*, 2001, **65**, 035406.
67. Google Books, CRC Handbook of Chemistry and Physics, 85th Edition, https://www.google.com/books/edition/CRC_Handbook_of_Chemistry_and_Physics_85/WDll8hA006AC?hl=en/.
68. J. K. Nørskov, J. Rossmeisl, A. Logadottir, L. Lindqvist, J. R. Kitchin, T. Bligaard and H. Jónsson, *Phys. Chem. B*, 2004, **108**, 17886-17892.
69. B. M. Wyvratt, J. R. Gaudet and L. T. Thompson, *J. Catal.*, 2015, **330**, 280-287.
70. S. R. J. Likith, C. A. Farberow, S. Manna, A. Abdulslam, V. Stevanović, D. A. Ruddy, J. A. Schaidle, D. J. Robichaud and C. V. Ciobanu, *J. Phys. Chem. C*, 2018, **122**, 1223-1233.
71. R. A. Mir, P. Sharma and O. P. Pandey, *Sci. Rep.*, 2017, **7**, 3518.
72. Y. Chen, H. Zhang, J. Zhang, J. Ma, H. Ye, G. Qian, Y. Ye and S. Zhong, *Mater. Sci. Appl.*, 2011, **2**, 1313.

73. N. S. Alhajri, D. H. Anjum and K. Takanabe, *J. Mater. Chem. A*, 2014, **2**, 10548-10556.
74. Z. Luo, R. Miao, T. D. Huan, I. M. Mosa, A. S. Poyraz, W. Zhong, J. E. Cloud, D. A. Kriz, S. Thanneeru, J. He, Y. Zhang, R. Ramprasad and S. L. Suib, *Adv. Energy Mater.*, 2016, **6**, 1600528.
75. C. Jian, Q. Cai, W. Hong, J. Li and W. Liu, *Small*, 2018, **14**, 1703798.
76. K. A. Goulas, A. V. Mironenko, G. R. Jenness, T. Mazal and D. G. Vlachos, *Nat. Catal.*, 2019, **2**, 269-276.
77. A. V. Mironenko and D. G. Vlachos, *J. Am. Chem. Soc.*, 2016, **138**, 8104-8113.